Journal of Materials Chemistry A

Boosting Electrochemical Reaction and Suppressing Phase Transition with High-Entropy O3-Type Layered Oxide for Sodium-Ion Batteries

Journal:	*Journal of Materials Chemistry A*
Manuscript ID	TA-ART-03-2022-002451.R2
Article Type:	Paper
Date Submitted by the Author:	01-Jun-2022
Complete List of Authors:	Tian, Kanghui; Northeastern University at Qinhuangdao He, Huan; Northeastern University at Qinhuangdao Li, Xiao; Northeastern University at Qinhuangdao Wang, Dan; Northeastern University at Qinhuangdao Wang, Zhiyuan; Northeastern University at Qinhuangdao, School of Resources and Materials Zheng, Runguo; Northeastern University at Qinhuangdao, Sun, Hongyu; Northeastern University at Qinhuangdao Liu, Yanguo; Northeastern University at Qinhuangdao Wang, Qinchao; Yangzhou University

Boosting Electrochemical Reaction and Suppressing Phase Transition with High-Entropy O3-Type Layered Oxide for Sodium-Ion Batteries

Kanghui Tian, [a] Huan He, [a] Xiao Li, [a] Dan Wang, [a,b] Zhiyuan Wang,*[a,b] Runguo Zheng, [a,b] Hongyu Sun, [b] Yanguo Liu, [a,b] Qin-Chao Wang *[c]

[a] School of Materials Science and Engineering, Northeastern University, Shenyang 110819, P.R. China;

[b] School of Resources and Materials, Northeastern University at Qinhuangdao, Qinhuangdao 066004, P.R.China;

[c] School of Chemistry and Chemical Engineering, Yangzhou University, Jiangsu 225002, P. R. China;

Corresponding author: (ZY W) zhiyuanwang@neuq.edu.cn; (Q-C W) wangqinchao@yzu.edu.cn

Abstract: The complex phase transitions induced by interlayer slide in layered cathode materials lead to poor cycling stability and rate capability for sodium-ion batteries. Herein, we design and prepare a new six-component high-entropy oxide (HEO) layered cathode O3-Na($Fe_{0.2}Co_{0.2}Ni_{0.2}Ti_{0.2}Sn_{0.1}Li_{0.1}$)$O_2$ to enable highly reversible electrochemical reaction and phase-transition behavior. The HEO cathode exhibits good cycling performance (capacity retention of ~81% after 100 cycles at 0.5 C) and outstanding rate capability (capacity of ~81 mAh g^{-1} at 2.0 C) due to the higher sodium diffusions coefficient (above 5.75×10^{-11} cm^2 s^{-1}) than most reported O3-type cathodes. Moreover, the high-entropy cathode has superior compatibility to hard carbon anode and delivers specific capacity of 90.4 mAh g^{-1} (energy density of ~267.5 Wh kg^{-1}). Ex-situ X-ray diffraction proves that the high-entropy designing effectively suppress the intermediate phase change to achieve reversible O3-P3 phase evolution, and in turn stabilize the layered structure. X-ray absorption spectroscopy and Mössbauer spectrum of ^{57}Fe suggest that $Ni^{2+}/Ni^{3.5+}$, $Co^{3+}/Co^{3.5+}$, and part of $Fe^{3+}/Fe^{3.5+}$ redox reaction contribute the charge compensation. The enhanced performance can be attributed to the disordered distribution of multi-component transition metals in HEO suppress the ordering of electric charge and sodium vacancy, thereby inhibiting the

interlayer slide and phase transition.

Keywords: Sodium-ion batteries, layered cathode, high-entropy oxide, phase transition

1. Introduction

Sodium-ion batteries (SIBs) have received extensive attention in scientific research and industrial fields because of the abundant reserves of sodium in the earth's crust and its low cost, which can meet the demand of large-scale energy storage [1-3]. However, the development of cathode materials seriously lags behind that of anode materials, which has become one of the limiting factors for future application of SIBs[4,5]. Currently, a series of cathode materials have been investigated to improve the energy/power density and cycling life of SIBs, such as transition metal oxides[6], polyanion compounds[7], Prussian blue analogues[8] and organic compounds[9]. Among them, the layered transition metal oxide Na_xTMO_2 ($x \leqslant 1$, TM=transition metal) is considered as one of the most promising cathode materials because of its high energy density and concise synthesis method [6,10]. In recent decades, researchers have prepared a variety of layered transition metal oxides Na_xTMO_2, such as environmentally friendly Fe-based (O3-$NaFeO_2$[11]) oxides; low-cost Mn-based (P2-$Na_{0.67}MnO_2$) [12], P2-$Na_{7/9}Cu_{2/9}Fe_{1/9}Mn_{2/3}O_2$[13]) and high-voltage Ni-based (O3-$NaNiO_2$[14], P2-$Na_{2/3}Ni_{2/3}Te_{1/3}O_2$[15], O3-$NaNi_{0.5}Mn_{0.3}Ti_{0.2}O_2$[16]) oxides.

In traditional transition metal oxides ($NaTMO_2$), the redox reaction is occurred from the active TM sites, which provides the charge compensation for sodium storage. Sodium ions transfer from one NaO_6 octahedral site to another via the adjacent tetrahedron, resulting in the formation of Na^+/vacancy superstructures in Na-poor phase, which can be observed though the Laue diffraction patterns[17-19]. At the same time, this desodiation process induces strong repulsion of oxygen, and the interlayer distance thus expands. Meanwhile, the TMO_2 slabs glides in the vectors of (1/3, 2/3, *z*) and (2/3, 1/3, *z*), progressing with structure transformation of O3→O'3→P3→P'3 [20,21]. Tuning the type and ratio of transition metal can reorganize the Na^+/vacancy superstructure and modify the structural evolution, which has a crucial impact on the reversible stability

and sodium diffusion rate during charge and discharge process[22-24]. What is exciting is that the electrochemical performance of these multi-component cathodes are significantly better than that of less-component materials, and it is easier to achieve the high energy density and long cycling life that researchers expect[25,26]. Therefore, in order to tailor the cathode material with high sodium-storage performance, multi-component or high-entropy layered oxides have attracted the attention of researchers.

High-entropy oxides (HEOs), as a new type of oxide system, have become a research hotspot due to its unique structure and excellent performance[27]. Generally, HEOs is considered as a solid-solution phase composed of five or more elements in equimolar or nearly equimolar ratios (each element content is between 5% and 35%), including rock salt, fluorite, spinel, and perovskite structures[28-30]. Due to the disorder arrangement of the multiple principal elements, HEOs exhibit excellent properties that traditional materials do not possess, such as superionic conductivity and excellent cycling stability [31-33]. Recently, the application of high-entropy oxides in the field of energy storage has attracted the attention of researchers. According to reports, Sarkar et al. applied the rock salt structured HEO $(Mg_{0.2}Co_{0.2}Ni_{0.2}Cu_{0.2}Zn_{0.2})O$ to the anode material of lithium-ion batteries for the first time, and showed that it has almost no capacity loss after 500 cycles[27]. In addition, they compared the electrochemical performance of medium-entropy materials, and revealed that the excellent structural stability and cycling stability of HEOs were attributed to higher configuration entropy. Wang et al. prepared a multi-anionic and multi-cationic high-entropy oxide Li(HEO)F on the basis of $(Mg_{0.2}Co_{0.2}Ni_{0.2}Cu_{0.2}Zn_{0.2})O$, which was used as cathode material for LIBs and had excellent capacity retention after 300 cycles[34]. Furthermore, Zhao et al. applied the concept of high-entropy chemistry to the design of cathode materials for SIBs[35]. They successfully prepared a nine-component O3-type layered high-entropy oxide $NaNi_{0.12}Cu_{0.12}Mg_{0.12}Fe_{0.15}Co_{0.15}Mn_{0.1}Ti_{0.1}Sn_{0.1}Sb_{0.04}O_2$ as a cathode material for SIBs, and the HEO cathode displays superior cycling stability (83% capacity retention after 500 cycles) and excellent rate performance (80% capacity retention at 5 C). Moreover, they also demonstrated that the high-entropy structure can delay the phase transformation behavior of Na^+ during the (de)intercalation, which is beneficial to

increase the specific capacity of cathode materials. The excellent storage performance of Li^+ and Na^+ may be related to the synergy function between multiple components in HEOs, which preserves the structure of the matrix during the (de)intercalation of Na^+.

Inspired by HEOs in electrochemical energy storage, we designed and successfully prepared a new type of six-component layered HEO O3-Na($Fe_{0.2}Co_{0.2}Ni_{0.2}Ti_{0.2}Sn_{0.1}Li_{0.1}$)$O_2$ (denoted as O3-NFCNTSL) for the first time as a cathode material for SIBs. Herein, two criteria were following to design the HEOs cathode: the disordering of TM and high electrochemical performance (detailed selection criteria for elements are given in supplementary information). The ionic radii difference of the selected element (Fe^{3+}, Ni^{2+}, Co^{3+}, Mn^{4+}, Ti^{4+}, Sn^{4+}) is smaller than 15% as shown in Table S1, so it is easily to synthesize the disordering of TM. While, the Ni^{2+}, Fe^{3+} and Co^{3+} can provide the charge compensation, which can enhance electrochemical performance. In addition, we systematically studied the electrochemical performance of O3-NFCNTSL. This material exhibits excellent cycling stability, and its capacity retains ~81% after 100 cycles at 0.5 C (1 C=100 mA g^{-1}). At the same time, it has excellent rate performance, with a reversible specific capacity of about 81 mAh g^{-1} at 2 C. Ex-situ XRD revealed that NFCNTSL not only suppresses the transition of intermediate phase, but also has a highly reversible O3-P3 phase transition behavior. Furthermore, the charge compensation mechanism of NFCNTSL was further studied by ex-situ XAS and Mössbauer spectrum of Fe. In the initial charge/discharge process, $Ni^{2+}/Ni^{3.5+}$ and $Co^{3+}/Co^{3.5+}$ redox reactions provide charge compensation while partly $Fe^{3.2+}/Fe^{3.5+}$ supplies the rest charge compensation. This work provides new insights for the application of HEOs in electrochemical energy storage.

2. Experimental Section

Materials Synthesis: The HEO Na($Fe_{0.2}Co_{0.2}Ni_{0.2}Ti_{0.2}Sn_{0.1}Li_{0.1}$)$O_2$ was prepared through a solid-state method. The raw materials (purchased from Aladdin Chemical Reagent Co., Ltd) of the synthetic samples are all analytical purity grade without further purification. According to the stoichiometric ratio of the elements, Na_2CO_3 (0.5 mol, 99.5%), Fe_2O_3 (0.1 mol, 99%), Co_3O_4 (0.067 mol g, 99%), NiO (0.2 mol, 99%), TiO_2

(0.2 mol, 99%), SnO_2 (0.1 mol, 99.5%), Li_2CO_3 (0.05 mol, 99.7%) powder were well mixed by a planetary ball mill. The obtained mixture was calcined at 900 °C for 12 h in a muffle furnace, and then cooling the sample to room temperature naturally. Finally, the sintered sample was ground to below 200 mesh by an agate mortar and immediately transferred into an Ar-filled glovebox.

Materials Characterization: The X-ray diffraction (XRD) patterns of the sample and electrode at various charge states (charging voltage: 2.0, 3.3, 3.5, 3.7, 3.9, 4.1 V; discharging voltage: 3.8, 3.5, 3.2, 3.0, 2.8, 2.5, 2.0 V) were collected by Rigaku Smartlab X-ray diffractometer (Cu Kα, λ = 0.15406 nm) at 45 kV and 200 mA. The crystal structure information of O3-NFCNTSL was analyzed by the GSAS-Ⅱ. The elemental composition of the materials were analysed through inductively coupled plasma optical emission spectrometer (ICPE-9800, ICP-OES). The morphology and element distribution of O3-NFCNTSL were observed through field-emission scanning electron microscope (FESEM, ZEISS SUPRA55) and the energy disperse spectroscopy (EDS) attached to the SEM. The HRTEM image and selected area electron diffraction (SAED) patterns were examined by transmission electron microscope (TEM, JEM 2100F). X-ray absorption spectroscopy (XAS) was carried out at beamline 7BM (QAS) of the National Synchrotron Light Source II (NSLS-II) at Brookhaven National Laboratory (BNL). Ni, Co, Fe, Ti K-edge XAS spectra were measured though transmission mode, with reference spectrums simultaneously collected using corresponding metal foil. The XAS data was analyzed using Athena and Artemis software packages [38,40]. The Mössbauer spectra were recorded at room temperature with a MS-96 Mark II spectrometer working in a constant acceleration mode, and the isomer shift was recorded with respect to the α-Fe metal. The experimentally obtained spectra were fitted using MOSSWIN software.

Electrochemical measurements: The working electrode was prepared by mixing active material (80 wt%), acetylene black (10 wt%), polyvinylidene fluoride (PVDF, 10 wt%), and an moderate amount of N-methylpyrrolidone (NMP) into a slurry, then coating the above slurry on the Al foil and drying it in a vacuum oven at 80 °C for 8 h. Subsequently, the working electrode was rolled and cut into a disc with a diameter of

14 mm. The average mass loading of active material is about 3.5 mg cm^{-2}. The electrochemical performance of the O3-NFCNTSL cathode was evaluated in the CR2032 coin cells, which assembled by using O3-NFCNTSL as the working electrode, Na metal as counter electrode, glass microfiber (Whatman, GF/D) filters as the separator and 1.0 M $NaClO_4$ dissolved in propylene carbonate (PC, 100 Vol%) with 5% fluroethylene carbonate (FEC) as the electrolyte in an Ar-filled glovebox. The galvanostatic discharge/charge and galvanostatic intermittent titration technique (GITT) test were carried out on LAND CT2001Asystem with a voltage window of 2.0~4.1 V. Cyclic voltammetry (CV) measurements were performed on the CHI1000C electrochemical workstation at different scan rates from 0.1 to 1.0 mV s^{-1} in a voltage range of 2.0~4.1 V (*vs*. Na^+/Na). Electrochemical impedance spectroscopy (EIS) measurements were performed using the Energylab XM electrochemical workstation with amplitude of 5 mV in the frequency range of 10^5 ~10^{-2} Hz. For the full-cell, the O3-NFCNTSL cathode and hard carbon (HC) anode were firstly assembled into half-cells and precycled for 3 cycles before assembled to full cells. In the full cell, the capacity ratio of cathode to anode was set as 1.2, and the weight ratio of two electrodes was balanced based on the discharge capacity of cathode and the charge capacity of anode in half-cells. The electrochemical performance of the full-cell was evaluated in the voltage range of 0.5~4.1 V.

3. Results and Discussion

The inductively coupled plasma atomic emission spectrometry (ICP-OES) was employed to examine the element ratios of the NFCNTSL. Table S2 shows that the ratio of Fe, Co, Ni, Ti, Sn is 0.20:0.21:0.22:0.20:0.10, which are almost consistent with the design ratio of various metal elements in the NFCNTSL. The XRD was performed to investigate the crystal structure and phase information of the as-prepared HEO NFCNTSL displayed in Fig. 1a. All the main diffraction peaks in the XRD pattern are well indexed to the α-$NaFeO_2$ structure with $R\bar{3}m$ space group (JCPDS: 82-1495), except for trace amount of NiO impurity. Based on the rhombohedral α-$NaFeO_2$ structure, the XRD pattern was analyzed by Rietveld refinement to further determine

the crystal structure information. Table S3 shows that the refined lattice parameters are $a=b$=2.994 Å, c=16.091 Å with unit cell volume of 124.94 Å^3. Fig. 1b displays the structure schematic of O3-NFCNTSL, in which Fe, Co, Ni, Ti, Sn and Li occupy the (0 0 0.5) sites. The metal cations combine with oxygen to form TMO_6 octahedrons, and sodium ions are located at the adjacent TMO_2 layers. Fig. 1c displays the SEM image of the synthesized O3-NFCNTSL, which are composed of irregular block particles with size of 3~5 μm. SEM-EDS in Fig. 1d and TEM-EDS in Fig. S1 mapping demonstrates that various elements of Na, Fe, Co, Ni, Ti, Sn, and O are uniformly distributed on the O3-NFCNTSL entire particles, without obvious segregation phenomenon. Furthermore, the results of SEM-EDS (Table S4) show that the measured atomic ratio of each element is close to the designed stoichiometry (Fe:Co:Ni:Ti:Sn=2:2:2:2:1), which is consistent with the ICP-OES result. The TEM image (Fig. 1e) also shows that the morphology of O3-NFCNTSL is micron-scale irregular particles. HRTEM and SAED measurements were used to further investigate the O3 phase as shown in Fig. 1f and Fig. 1g, respectively. The interplanar distance between the adjacent lattice fringes is measured to be 0.53 nm, consistent with the (003) *d*-space of layered hexagonal structure. Meanwhile, Fig. S2 shows that the neighboring distance of the (101) crystallographic plane is 0.256 nm, further confirming the high crystallinity of HEO O3-NFCNTSL. The bright diffraction rings in the SAED image in Fig. 1g correspond to (003), (006), (104), and (110) crystal planes, respectively, suggesting that the as-prepared HEO NFCNTSL has a perfect O3 type lattice structure.

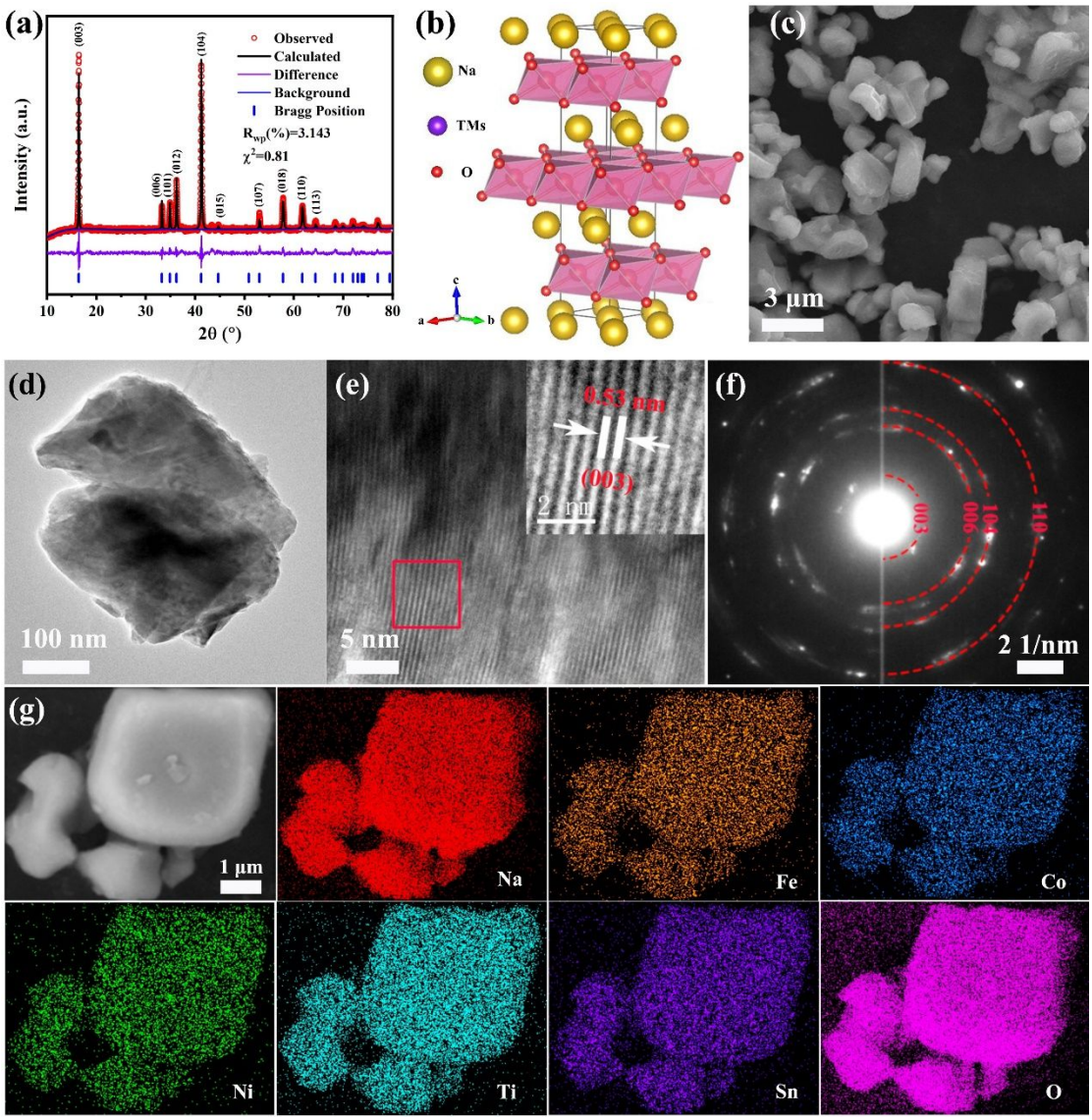

Fig. 1 Structure and morphology of as-prepared HEO O3-NFCNTSL cathode. (a) XRD and Rietveld pattern. (b) Structure schematic. (c) SEM image. (d) and (e) TEM and HRTEM image (f) SAED pattern. (g) SEM-EDS mapping.

The electronic and local structure of transition metal (Fe, Co, Ni, and Ti) in the O3-NFCNTSL was analyzed by synchrotron X-ray absorption spectroscopy (XAS). Fig. 2a-d reveals the X-ray absorption near edge structure (XANES) spectra of Fe, Co, Ni and Ti K-edges in pristine O3-NFCNTSL, respectively, along with the standard reference compounds Fe_2O_3 (Fe^{3+}) and Fe_3O_4 ($Fe^{2.67+}$), $LiCoO_2$ (Co^{3+}) and Co_3O_4 ($Co^{2.67+}$), NiO (Ni^{2+}) and $LiNiO_2$ (Ni^{3+}), TiO (Ti^{2+}) and TiO_2 (Ti^{4+}), respectively. Generally, the threshold energy position in the K-edge XANES spectra of the targeted transition metals is sensitive to their chemical valence states, while the shape of the

peaks is powerful for determining the coordination environment of the absorbing element[36,37]. Comparing with the metal oxide references, it can be deduced that the original average valences of Fe, Co, Ni, and Ti in as-prepared O3-NFCNTSL are primarily determined as 3+, 3+, 2+, and 4+, respectively.

The magnitudes of the Fourier-transformed extended X-ray absorption fine structure (FT-EXAFS) spectra of various transition metals (TM= Fe, Co, Ni, and Ti) in O3-NFCNTSL and corresponding least-squares fitting are displayed in Fig. 2e-h. In Fig. 2e-h, there are two main effective scattering paths, the first peak at R≈1.5-1.6 Å is indexed as the shortest six-equidistant oxygen around targeted absorbing TM, forming the nearest TMO_6 octahedral, and the second peak at R≈2.6 Å is indexed as the TM-TM_6 hexagon in the *a-b* plane of the second coordination shell[38,39]. In fact, because of not phase corrected, the distance of two atoms in FT-EXAFS spectra is about 0.3-0.4 Å shorter than the actual bond lengths [40,41]. Table S5 shows the detailed structure information derived from simulating the FT-EXAFS in the model of the hexagonal $R\bar{3}$ *m* space group. In Table S5, Ni-O shows the longest lengthen and highest Debye-Waller factors (δ) for the first TM-O coordination, relating to the large ionic radius and the activity of low spin $Ni^{2+}(t_{2g}^6e_g^2)$ ions. It is interesting that both the *R* and δ value for Fe-O are larger than that of low spin Co^{3+}($t_{2g}^6e_g^0$). It is well known that the ionic radius of high spin Fe^{3+} (0.645 Å), larger than low spin Fe^{3+} (0.55 Å) and low spin Co^{3+} (5.45 Å). It is rational to conclude that Fe in O3-NFCNTSL is dominated by high spin Fe^{3+}. The Mössbauer spectrometer was used to further investigate the properties of Fe^{3+} in O3-NFCNTSL.

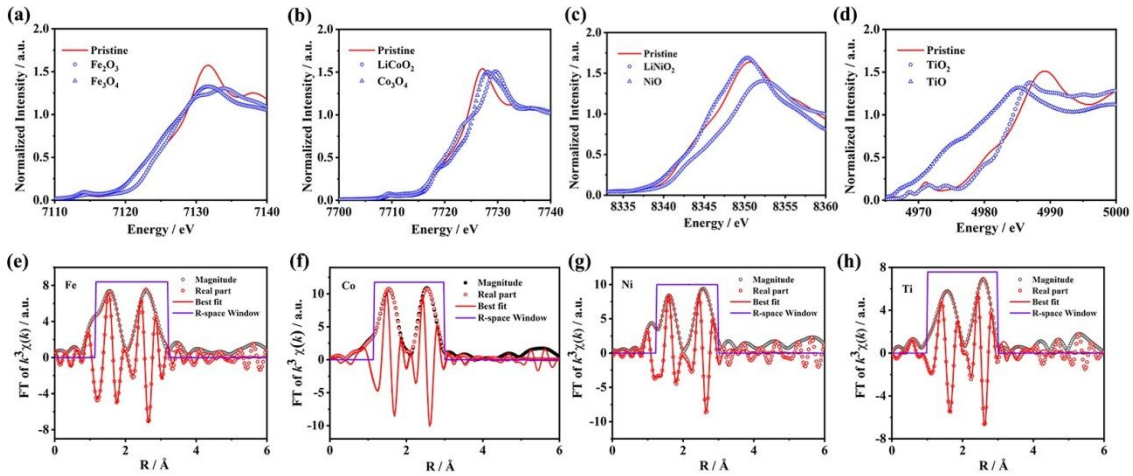

Fig. 2 XANES spectra of the (a) Fe, (b) Co, (c) Ni, and (d) Ti K-edge of pristine O3-NFCNTSL and related metal oxide references, including Fe_2O_3, Fe_3O_4, Co_3O_4, $LiCoO_2$, NiO, $LiNiO_2$, TiO, and TiO_2. The least-square fits of the calculated FT-EXAFS phase and amplitude functions to the experimental EXAFS spectra for (e) Fe, (f) Co, (g) Ni, and (h) Ti in O3-NFCNTSL.

The electrochemical performance of O3-NFCNTSL was evaluated in Na//O3-NFCNTSL half-cell at 0.1 C (10 mA g^{-1}). To further optimize the voltage window, galvanostatic charge/discharge (GCD) tests at different cut-off voltages (4.0 V, 4.1 V, and 4.2 V) were performed as shown in Fig. S3, Fig. 3a, and Fig. S4, respectively. Fig. S3 shows the best cycling stability of O3-NFCNTSL between 2.0 to 4.0 V, but the low cut-off voltage limits the extraction of Na ions, resulting in a low reversible specific capacity of 90 mAh g^{-1}. Although displaying the highest initial charging specific capacity of 130.6 mAh g^{-1} at 2.0-4.2 V, O3-NFCNTSL cathode leads to the poorest reversible specific capacity (only 98.3 mAh g^{-1}), corresponding to the initial Coulombic efficiency (CE) is about 75% (Fig. S4). Moreover, the reversible specific capacity decreased to 84.4 mAh g^{-1} only after 10 cycles. The large capacity loss may be related to the irreversible voltage platform above 4.1 V. When the voltage window is set to 2.0-4.1 V, as shown in Fig. 3a, the GCD curves almost coincide, and the initial charge and discharge specific capacity is 137.7 mAh g^{-1} and 112.7 mAh g^{-1} with an initial CE of about 81.8 %, which corresponds to ~0.57 Na^+ extraction and ~0.47 Na^+ insertion, respectively. It shows that the O3-NFCNTSL cathode has the best reversible capacity and excellent cycle stability at 2.0-4.1 V (*vs.* Na^+/Na), and the electrochemical performance is further studied under this voltage window. The dQ/dV plots (Fig. 3b)

of the initial three cycles show a similar shape with two pairs of peaks at 3.10/2.99 V and 3.63/3.55 V, indicating the excellent cyclic reversibility of O3-NFCNTSL. Furthermore, the small voltage polarization (at ~0.11 V and ~0.08 V) suggests that the O3-NFCNTSL cathode has good kinetic properties. The cyclic voltammetry (CV) test in Fig. S5 future indicates that the curves of O3-NFCNTSL cathode are almost coincide except for the first cycle, exhibiting excellent reversibility. Based on previous conclusions, the peak couple at 3.12/2.94 V (*vs.* Na^+/Na) could be attributed to the redox reaction of Ni^{2+}/Ni^{3+}, and the broad peak couple at 3.7/3.53 V might be assigned to the redox reaction of Fe^{3+}/Fe^{4+} and Co^{3+}/Co^{4+}[42,43]. In contrast, Ti^{4+} and Sn^{4+} are electrochemically inactive in the voltage range of 2.0-4.1 V (*vs.*Na^+/Na) [44,45]. Therefore, it is preliminarily determined that Fe, Co, and Ni provide charge compensation during the Na^+ intercalation/deintercalation. The detailed charge compensation mechanism will be discussed in the ex-situ XAS section. Fig. 3c and Fig. 3d exhibit the rate capability of the O3-NFCNTSL cathode. As shown in Fig. 3c, O3-NFCNTSL cathode deliver reversible capacities of 112.7, 103.8, 95.2, 88.5, and 80.8 mAh g^{-1} at 0.1, 0.2, 0.5, 1 and 2 C, respectively. It should be noted that the Coulombic efficiency can be maintained at ~98% at different rates, indicating that O3-NFCNTSL cathode has outstanding reversibility for sodium storage. In addition, when the current density returned to 0.1 C, the reversible capacity of O3-NFCNTSL electrode recovered to 111.0 mAh g^{-1}, revealing superior rate stability and excellent kinetic performance. In Fig. 3d, it can be seen that the discharge platform of the O3-NFCNTSL electrode gradually weakens and moves downward as the current density increases. Thus, this as-synthesized O3-NFCNTSL electrode exhibits superior quick-sodiation performance. The cycling performance of the O3-NFCNTSL cathode is shown in Fig. 3e and Fig. 3f. The O3-NFCNTSL cathode exhibits an outstanding cycling stability with a reversible capacity of 81.4 mAh g^{-1} after 100 cycles at 0.1 C (capacity retention of ~72%) in Fig. 3e and 65 mAh g^{-1} after 200 cycles at 0.5 C (capacity retention of ~67%) in Fig. 3f. The excellent electrochemical performance is higher than most cathode materials of SIBs recently reported, as show in Table S8. It is noteworthy that the O3-NFCNTSL cathode has not taken any optimization and modification measures (such as coating conductive

materials, reducing particle size, and surface modifications, etc.), so its electrochemical performance can be further improved.

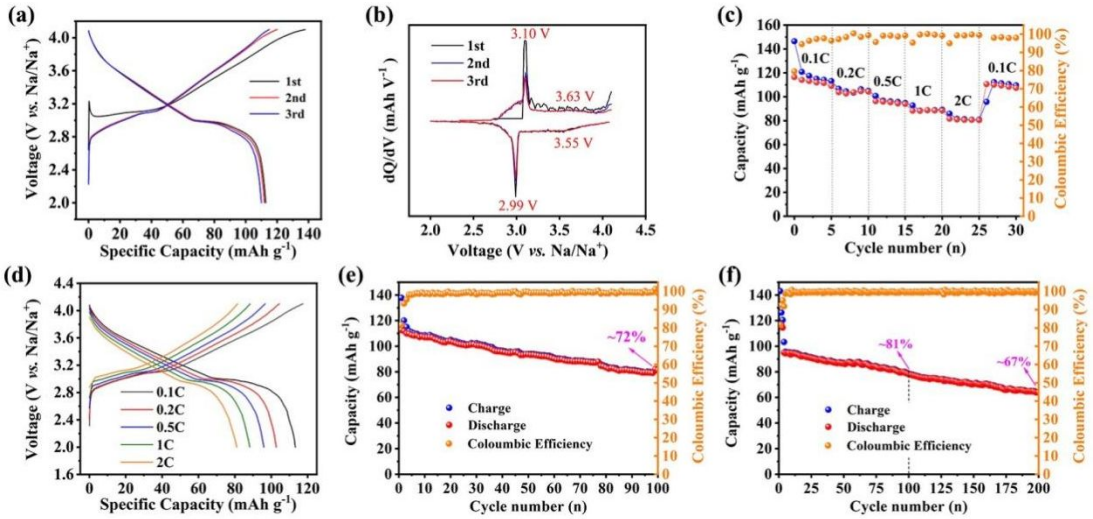

Fig. 3 (a) Galvanostatic charge/discharge profiles of O3-NFCNTSL cathode in voltage range of 2.0-4.1V at 0.1 C. (b) The dQ/dV plots for first three cycles at 0.1 C derivated from (a). (c) Rate capability of O3-NFCNTSL cathode at various rates. (d) Galvanostatic charge/discharge curves of O3-NFCNTSL cathode at different rates. (e and f) Cycling performance of O3-NFCNTSL cathode at 0.1 C and 0.5 C.

The Na^+ transport kinetic properties of O3-NFCNTSL cathode were investigated by CV measurement and galvanostatic intermittent titration technique (GITT). Fig. 4a reveals the CV curves for O3-NFCNTSL cathode at different scanning rates from 0.1 to 1.0 mVs^{-1}. With the increase of scan rate, the peaks display a linear shift as shown in Fig. 4b (the fitting information is shown in Table S9), implying a diffusion-controlled behavior of sodium-ion transport in O3-NFCNTSL [2]. The Na^+ apparent diffusion coefficient (D_{Na^+}) of the O3-NFCNTSL cathode is estimated according to the Randles-Sevcik equation. The values of D_{Na^+} are calculated to be 2.86×10^{-11} cm^2 s^{-1} and 3.44×10^{-11} cm^2 s^{-1} for the charge and discharge processes, respectively (supporting information). In addition, GITT was used to further evaluate the diffusion coefficient of Na^+. Fig. 4c shows a clear linear relationship between the voltage and the square root of the galvanostatic time, with the detail galvanostatic titration process in the inset and fitting results in Table S10. The GITT curves and calculated D_{Na^+} in the O3-NFCNTSL cathode during the first cycle is displayed in Fig. 4d. During the entire galvanostatic

titration process, the average diffusion coefficient of Na^+ is about 5.75×10^{-11} cm^2 s^{-1}, which is significantly higher than most cathode materials for sodium ion batteries recently studied, as show in Table S11. The initial decrease of D_{Na^+} value may be related to sluggish transferring of Na^+ in O3 structure, which should overcome the energy barrier at the adjacent tetrahedron. However, sodium ions can quickly go through the two-dimensional bottleneck formed by oxygen cage in the P3 structure [17], which corresponds to the slope region on the GCD curves. It is worth noting that the diffusion coefficient shows good symmetry during the charge and discharge process, which implies the remarkable reversibility of sodium ion diffusions. Prominent diffusivity provides the basis for excellent rate performance for as-synthesized O3-NFCNTSL.

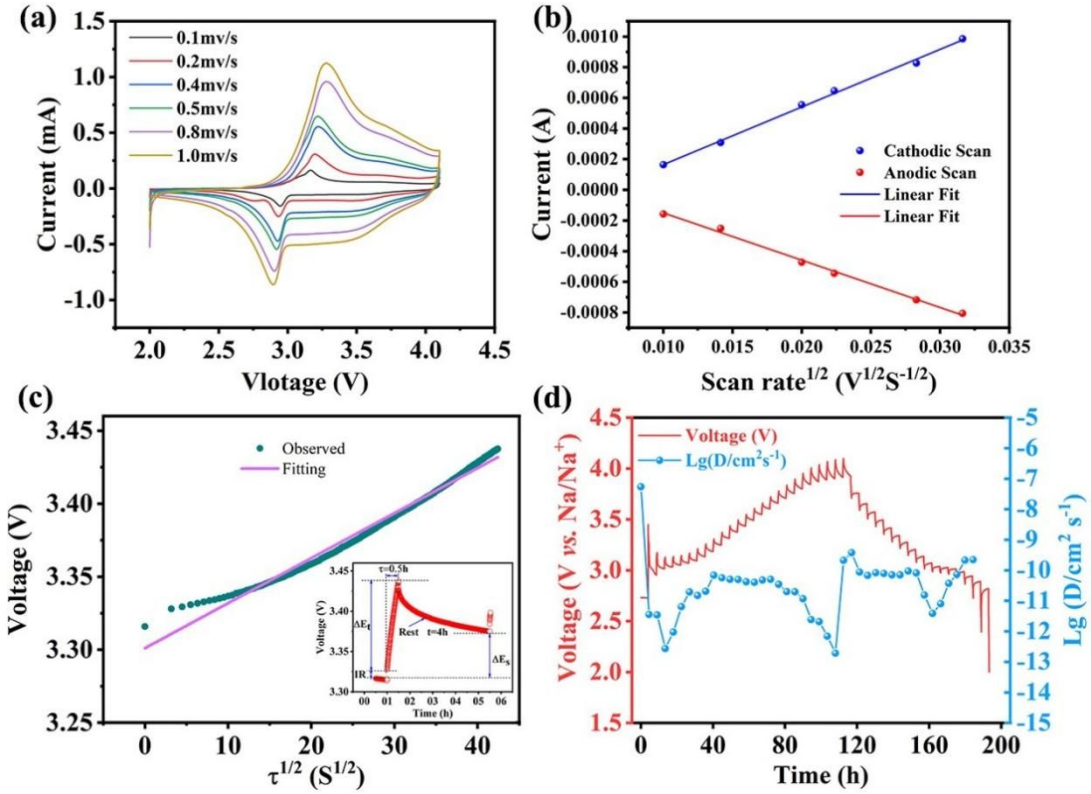

Fig. 4 The kinetics performance of Na^+ transferring in O3-NFCNTSL cathode. (a) CV curves of O3-NFCNTSL at different scan rates from 0.1 to 1.0 mv s^{-1}. (b) Liner relationship of peak currents with the scanning rate obtained from the CV measurements. (c) The linear relationship between the voltage and $\tau^{1/2}$ during galvanostatic intermittent titration states. The inset shows the detailed information for typical titration process. (d) GITT curves and Na^+ diffusivity as a function of voltage of O3-NFCNTSL cathode material in the first cycle.

In order to further uncover the structure evolution of O3-NFCNTSL cathode during the Na^+ (de) intercalation, *ex-situ* XRD patterns were collected at various voltage states during the first charge/discharge process within 2.0-4.1 V at 0.05 C, as shown in Fig. 5. Fig. S6 shows the corresponding charge and discharge states where the plots for ex-situ XRD patterns are collected. Before charging to 3.1 V, although the (003) and (006) peak continuously shifted to the lower 2θ angle, no new phase was observed. So, NFCNTSL cathode still keeps the O3 phase accompanied by *c* axis expansion as shown in Fig. 5c. Between 3.3 V ~ 3.5 V, both (003) and (104) peaks of the O3 phase gradually decreases, while the (003) and (015) peaks of the P3 phase grow sharp, suggesting that O3 phase transfer to P3 structure. With more Na^+ extracted from the host structure, the (003) peak of the O3 phase was completely replaced by the (003) peak of the P3 phase at 3.7 V, revealing that the structure evolved into a single P3 phase. In the range of 3.7~4.1 V, the (003) peak of the P3 phase shift to lower 2θ angle without impurity peaks, indicating that the Na^+ extraction behavior in this region is a solid solution reaction. Moreover, the structure evolution during discharging is completely opposite to the charging process. When discharged to 2.0 V, all diffraction peaks return to the original O3 phase, indicating that the O3-NFCNTSL structure is completely reversible. With the deintercalation of Na^+, the (003) and (006) shift to lower 2θ angle while the (101) and (012) shift to higher 2θ angle, which means that the lattice parameter *c* is continuously increases but *a*(*b*) is gradually decreases. The opposite change behavior of *a(b)* and *c* compensates for the change of the lattice volume and enhances the structural stability. The lattice parameters evolution of O3-NFCNTSL as a function of voltage is shown in Fig. 5b and Fig. 5c. During the charging process, the active elements are oxidized and their ion radius is reduced, resulting in the contract of the *ab*-plane. Meanwhile, the *c*-axis is expanding due to an increasing of the electrostatic repulsion between adjacent oxygen layers. In the fully discharged state, however, the values of the lattice parameters *a*(*b*) and *c* are almost the same as the initial state. The unit cell volume changes of Na^+ before and after (de)intercalation is only -0.22% (details in Table S12), which matches the excellent cycle stability. Notably, O3′, O3″, and P3′ phases generally exist in typical O3 cathode [46,47], for example O3-$NaMn_{0.5}Ni_{0.5}O_2$[48].

While, these phases was not observed in as-synthesized O3-NFCNTSL cathode during the entire desodiation and sodiation process. It can be concluded that designing HEOs oxides is conductive to suppressing phase transition and enhancing cycling stability of layered cathode materials.

To further valuate to the cycling stability, the structure and morphology of O3-NFCNTSL electrode after 100 cycles was characterized as shown in Fig. S7. In Fig. S7a, it is clearly observed the characteristic peaks of O3 phase in the XRD pattern, but no other impurity peaks. So, the O3-NFCNTSL cathode has robust structural stability after 100 cycles. However, due to the continuous evolution of O3-P3 phase transition, there are some cracks appearing on the surface of O3-NFCNTSL particles in Fig. S7b, which may be the main reason for the deterioration of electrochemical performance. Fig. S7c shows the EDS-mapping of O3-NFCNTSL electrode after the 100 cycles, where the elements Na, Fe, Co, Ni, Ti, Sn, and O are still evenly distributed, suggesting that the HEOs material has excellent structural stability.

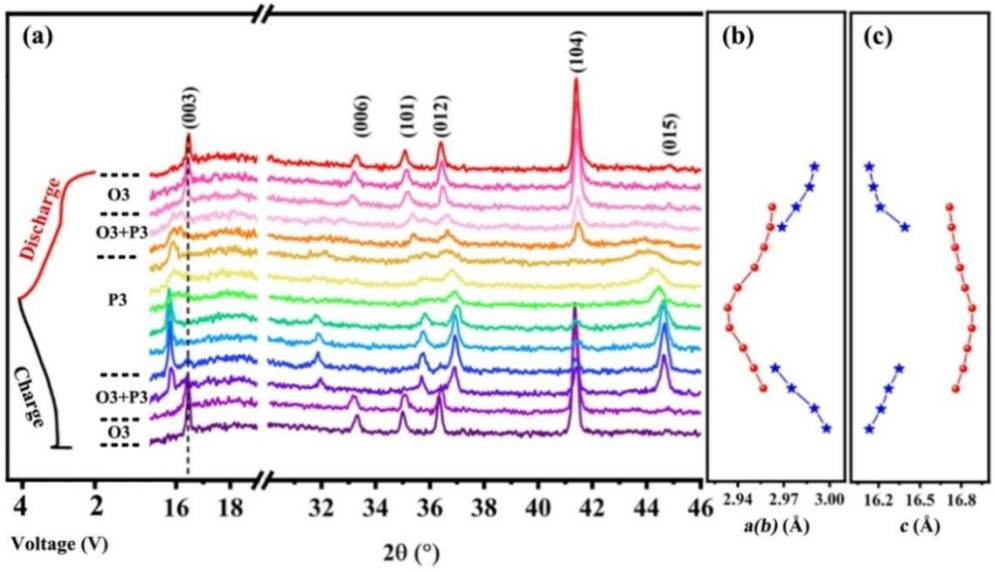

Fig. 5 (a) Ex-situ XRD patterns of the O3-NFCNTSL electrode during the initial charge/discharge processes and the corresponding voltage profiles during XRD data collections; (b and c) The evolution of lattice parameters $a(b)$ and c along with the voltage, derived from the XRD data according to the $R\bar{3}m$ (O3 and P3 phase) space groups.

In addition to structure changes, the charge compensation of and the evolution of local structure upon Na ions extraction/insertion of O3-NFCNTSL was also

investigated using ex-situ XAS spectra collected at K-edge of Fe, Co, and Ni. Fig. S8 shows the charge-discharge curves and the corresponding states where the plots for XAS scans are collected. Because the potential of Ti^{3+}/Ti^{4+} and Sn^{4+}/Sn^{5+} redox reaction low to 2.0 V[49,50], XANES spectra for Ti and Sn K-edge are ignored. Fig. 6a-f displays the normalized XANES spectra of Fe, Co and Ni K-edges at different charge and discharge states during the initial charge and discharge process. For the initial charge process, the white line of Ni K-edge in Fig. 6c continue to shift toward high energy at entire charge, suggesting Ni cations is oxidized to higher valence states. Because the white line of Ni K-edge at 4.1 V is higher than that of the standard reference of $LiNiO_2$ (Ni^{3+}), it is estimated that Ni^{2+} is oxidized to about +3.5 state in Fig. 6c at 4.1 V. The results show that about 0.3 e^- is extracted from low spin $Ni^{2+}(t_{2g}^6e_g^2)$, providing about 72 mAh g^{-1} capacity at the charging process. Besides, in Fig. 6a and b, the XANES spectra of Fe and Co are distorted during the whole desodiation process, with slight K-edge shifted. Thus, both Fe and Co provide the charge compensation for partial capacity. Thus, both Fe and Co are oxidized to +3.5, total providing 48 mAh g^{-1} capacity. Therefore, during initial charge process, Ni^{2+}, Co^{3+}, and Fe^{3+} are oxidized to $Ni^{3.5+}$, $Co^{3.5+}$ and $Fe^{3.5+}$, providing about 72, 24, and 24 mAh g^{-1} capacity, respectively.

In the first sodiation process (Fig. 6d-f), $Ni^{3.5+}$, $Co^{3.5+}$ and $Fe^{3.5+}$ are reduced, with all three metal's K-edge shift back to low absorbed energy. After discharge to 3.0 V, the energy of Ni K-edge continues to shift to low energy until to discharge to 2.0 V. However, from 3.0 V to 2.0 V, the white line of Co and Fe does not move or distort. It can be estimated that $Ni^{3.5+}$ is reversibly reduced to Ni^{2+}, providing about 0.3 e^- for charge compensation. From 4.1 V to 3.0 V, an average of 0.1 e^- was provided though Co reducing reaction during discharge, total supplying about 24 mAh g^{-1} discharge capacity. Although, Fe^{3+} is oxidized to $Fe^{3.5+}$ at first charge process correspongding 24 mAh g^{-1}, only part $Fe^{3.5+}$ was reduced to Fe^{3+} with the final average valence about +3.2, sacrificed about 9.6 mAh g^{-1} capacity during the first discharge. From 3.0 V to 2.0 V, no Fe or Co is reduced, only Ni ions are reduced. Therefore, a total number of 0.46 mol Na^+ is inserted into per mole of O3-NFCNTSL during the first discharge process, which agrees well with the initial discharge capacity of ~112 mAh g^{-1}.

In order to exactly analyze the charge compensation by Fe, Mössbauer spectrum of ^{57}Fe was performed. The Mössbauer spectrum of the original O3-NFCNTSL electrode is fitted using only a doublet, which is mainly assigned to Fe^{3+} located at octahedral site (coordination number 6). When charged to 4.1 V (Fig. 6h), the extraction/insertion of Na^+ upon charging yields an asymmetry of the doublet with increased spectral weight at velocity of about 0, revealing part of Fe^{3+} is oxidized to Fe^{4+}, which is consistent with XANES results in Fig. 6a and d. It further indicates that the Fe^{3+} in HEO O3-NFCNTSL structure is electrochemically active based on the Fe^{3+}/Fe^{4+} redox couple and involved in the charge compensation. In the discharged HEO O3-NFCNTSL cathode (Fig. 6i), there is no significant evidence of high spin Fe^{4+} O_6 and most of the Fe^{4+} ions are reduced. However, there is a clear difference in spectrum between the fully discharged electrode (Fig. 6i) and the original sample (Fig. 6h), manifesting the electronic structure of Fe in HEO O3-NFCNTSL cathode has not recovered completely after the first cycle. This change in Mössbauer spectrum may be due to two aspects. On the one hand, a small amount of Fe^{4+} has not been reduced after the first cycle and resulted in the initial irreversible capacity. On the other hand, a slight lattice distortion occurred in HEO O3-NFCNTSL structure induced by Na^+ extraction/insertion, as shown in Fig. 5b and c.

FT-EXAFS spectra present the characters of element-dependent property, which further observes the short-range local structure evolution for the targeted absorbing atom. The local environment changes near Fe, Co, and Ni ions in O3-NFCNTSL are shown in Fig. S9-S13. The first peak at about 1.6 Å is indexed as the distance of TM-O bond in TM-O_6 octahedra, while the second peak at about 2.5 Å presents the TM–TM interaction of TM–TM_6 hexagon in the *a*-*b* plane. As shown in Fig. S9-S13 (Table S5-S7), it is easily observed that the distance for the first coordination of Co-O, Fe-O and Ni-O all decreases during charge process, and increase for discharge process, suggesting the structural evolution of *d* and *p* hybrid orbital between transition metal and oxygen. It is noted that the two peaks for Ni reflecting the first and second coordination shells are more significant than those for Co and Fe, suggesting remarkable Jahn-Teller effect of Ni^{3+}. During the charge process, both TM-O and TM-

TM distances decrease, implying that Ni^{2+}, Co^{3+}, and Fe^{3+} are oxidized to shrink TMO_6 octahedra. While, the bond of TM-O and TM-TM are increased reversibly because of the reducing reaction, consisting with the results of XRD in Fig. 5b. The change of short-range TM-O and TM-TM strong reflects the evolution of crystal parameter of *a* and *b*.

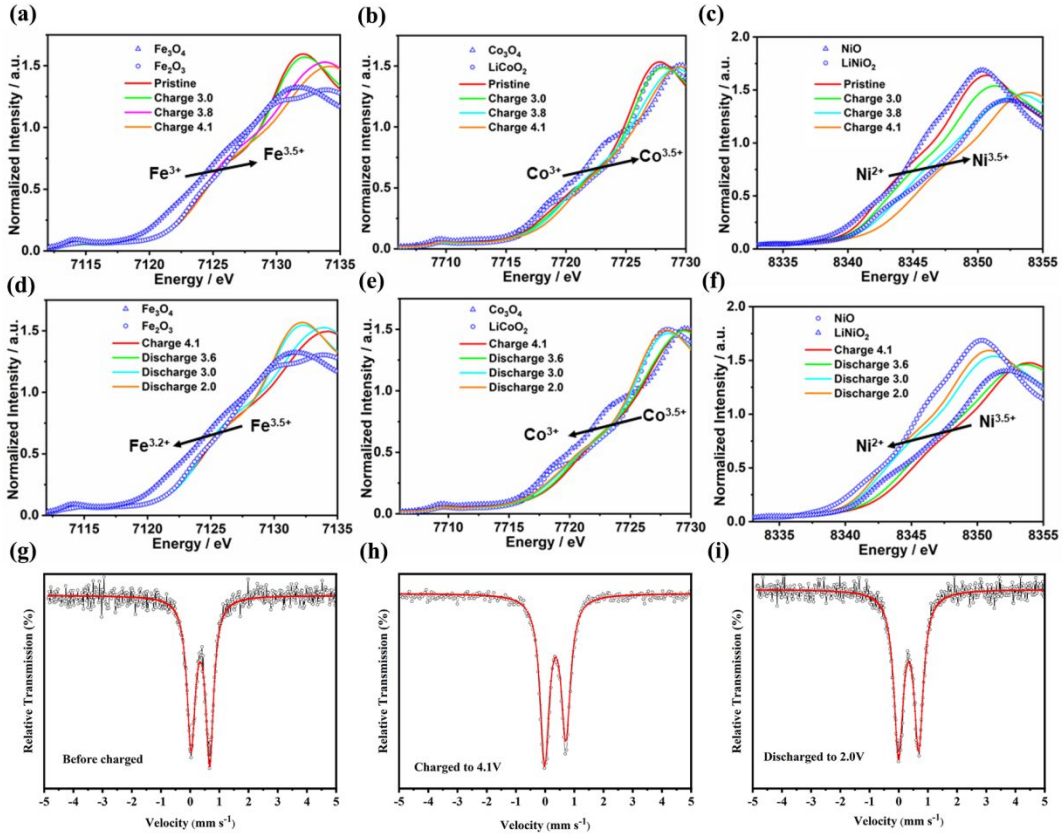

Fig.6 Ex situ XANES spectra at the (a, d) Fe K-edge, (b, e) Co K-edge, and (c, f) Ni K-edge of O3-NFCNTSL electrodes collected at different charge/discharge states. (g-i) Mössbauer spectrum of Fe.

In addition, to further reveal the practical potential of the O3-NFCNTSL cathode, the full cell was assembled with O3-NFCNTSL as cathode and hard carbon (HC) as anode. The structure and morphology of HC are shown in Fig. S14 and Fig. S15 respectively. Fig.7a exhibits the working mechanism schematic of sodium-ion full cell. Fig. 7b shows that the HC anode delivers ~293 mAh g^{-1} reversible capacity and the capacity retention is ~95% after 50 cycles (Fig. S16) at 20 mA g^{-1}, indicating that HC has excellent sodium storage performance. As shown in Fig. 7c, the O3-NFCNTSL//HC full cell delivers a reversible specific capacity of 90.4 mAh g^{-1}, which corresponds to

energy density of 267.5 Wh kg^{-1} (calculated based on the mass of the cathode active material) in 0.5-4.1V voltage at 5 mA g^{-1}. Fig. 7d suggests that O3-NFCNTSL/HC full cell exhibits excellent the capacity retention stability (about 71% after 50 cycles at 20 mA g^{-1}), demonstrating that the as-synthesized O3-NFCNTSL have superior compatibility to HC anode for practical prospects.

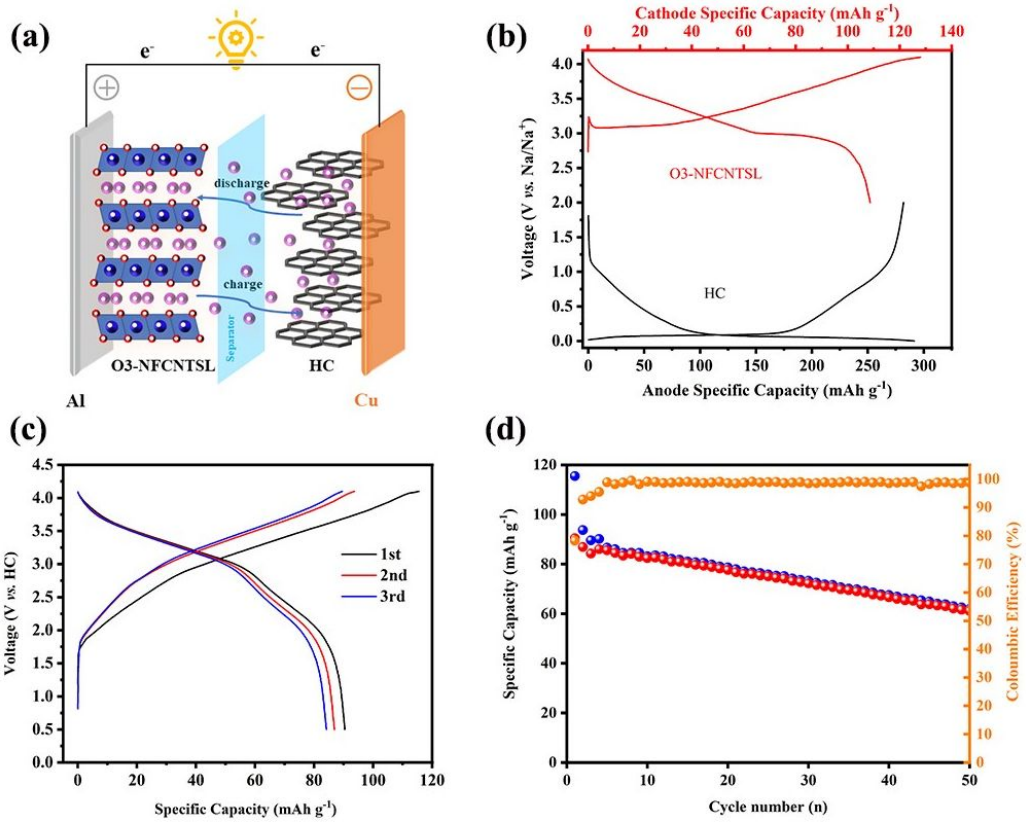

Fig. 7 Electrochemical properties of the O3-NFCNTSL//HC full cell systerm. (a) Working mechanism schematic of the full cell. (b) Galvanostatic charge/discharge curves of the O3-NFCNTSL cathode and HC anode *vs.* Na^+/Na. (c) Galvanostatic charge/discharge curves of the full cell at a current density of 5 mA g^{-1} in the voltage window of 0.5-4.1V *vs.* HC. (d) Cycling performance of the full cell at a rate of 20 mA g^{-1} in the voltage window of 0.5-4.1V *vs.* HC.

4. Conclusion

In this paper, a novel high-entropy O3-$Na(Fe_{0.2}Co_{0.2}Ni_{0.2}Ti_{0.2}Sn_{0.1}Li_{0.1})O_2$ cathode has been successfully synthesized for sodium-ion batteries, which can effectively suppress the structure change and enhance the reversible capacity and stable cycling capability. The high-entropy oxide O3-NFCNTSL composes six elementals, which can achieve the transition metal disordering, charge disordering and Na^+/vacancy

disordering. The resulted high-entropy oxide O3-NFCNTSL cathode delivers about 112.7 mAh g^{-1} reversible capacity at 0.1 C, long cycling stability (~72% of capacity retention after 100 cycles), and the outstanding rate capability (~71.7% of capacity retention at the rate of 2.0 C). Both CV and GITT measurements prove that the O3-NFCNTSL has much higher sodium diffusion rate (about 5.75×10^{-11} cm^2 s^{-1}), which is higher than the most reported O3-type layered oxides. Our synthesized O3-NFCNTSL has superior compatibility to HC anode, which delivers 90.4 mAh g^{-1} specific capacity (energy density of about 267.5 Wh kg^{-1}). The high-entropy designing can effectively suppress the inferior intermediate phase change to achieve O3-P3 phase evolution, enhancing the structure stability and achieving superior long-cycling stability. Furthermore, the ex-situ XAS and Mössbauer spectrum of ^{57}Fe indicate that $Ni^{2+}/Ni^{3.5+}$, $Co^{3+}/Co^{3.5+}$, and part of $Fe^{3+}/Fe^{3.5+}$ redox reaction contributes the charge compensation. Our work manifests that multi-metal high-entropy design is an effective strategy to develop high-performance cathode materials for SIBs.

Conflics of interest

There are no conflicts to declare.

Acknowledgements

This study was financially supported by the National Natural Science Foundation of China (No. 52071073, 51902046, 52071085, 51871046, 52171202, 52177208, and 51971055), Natural Science Foundation of Hebei Province (No. E2020501004), the Fundamental Research Funds for the Central Universities (N2123032). The authors thank beamlines 7-BM (QAS) of the National Synchrotron Light Source II, a U.S. Department of Energy (DOE) Office of Science User Facility operated for the DOE Office of Science by Brookhaven National Laboratory under Contract No. DE-SC0012704.

References

[1] S. Guo, P. Liu, H. Yu, Y. Zhu, M. Chen, M. Ishida and H. Zhou, Chem. Int. Ed.,

2015, **54**, 5894-5899.

[2] F. Ding, C. Zhao, D. Zhou, Q. Meng, D. Xiao, Q. Zhang, Y. Niu, Y. Li, X. Rong and Y. Lu, Energy Stor. Mater., 2020, **30**, 420-430.

[3] J. L. Yue, W. W. Yin, M. H. Cao, S. Zulipiya, Y. N. Zhou and Z. W. Fu, ChemComm, 2015, **51**, 15712-15715.

[4] T. Chen, J. Guo, Y. Zhuo, H. Hu, W. Liu, F. Liu, P. Liu, J. Yan and K. Liu, Mater., 2019, **20**, 263-268.

[5] M. Leng, J. Bi, W. Wang, Z. Xing, W. Yan, X. Gao, J. Wang and R. Liu, J. Alloys Compd., 2020, **816**, 152581.

[6] K. Kubota, N. Yabuuchi, H. Yoshida, M. Dahbi and S. Komaba, MRS Bull., 2014, **39**, 416-422.

[7] Y. Qi, Z. Tong, J. Zhao, L. Ma, T. Wu, H. Liu, C. Yang, J. Lu and Y. S. Hu, Joule, 2018, **2**, 2348-2363.

[8] Y. You, X. Yu, Y. Yin, K. W. Nam and Y. G. Guo, Nano Res., 2015, **8**, 117-128.

[9] L. Zhao, J. Zhao, Y. S. Hu, H. Li, Z. Zhou, M. Armand and L. Chen, Adv. Energy Mater., 2012, **2**, 962-965.

[10] M. H. Han, E. Gonzalo, G. Singh and T. Rojo, Energy Environ. Sci., 2015, **8**, 81-102.

[11] N. Yabuuchi, H. Yoshida and S. Komaba, Electrochemistry, 2012, **80**, 716-719.

[12] B. Peng, Z. Sun, S. Jiao, G. Wang and G. Zhang, Batteries Supercaps, 2020, **3**, 147-154.

[13] Y. Li, Z. Yang, S. Xu, L. Mu, L. Gu, Y. S. Hu, H. Li and L. Chen, Adv. Sci., 2015, **2**, 1500031.

[14] L. Wang, J. Wang, X. Zhang, Y. Ren, P. Zuo, G. Yin and J. Wang, Nano Energy, 2017, **34**, 215-223.

[15] A. Gupta, C. B. Mullins and J. B. Goodenough, J. Power Sources, 2013, **243**, 817-821.

[16] H. Wang, M. Gu, J. Jiang, C. Lai and X. Ai, J. Power Sources, 2016, **327**, 653-657.

[17] G. Shu and F. Chou, Phys. Rev. B, 2008, **78**, 052101.

[18] M. Roger, D. Morris, D. Tennant, M. Gutmann, J. Goff, J. U. Hoffmann, R. Feyerherm, E. Dudzik, D. Prabhakaran and A. Boothroyd, Nature, 2007, **445**, 631-634.

[19] M. Medarde, M. Mena, J. Gavilano, E. Pomjakushina, J. Sugiyama, K. Kamazawa, V. Y. Pomjakushin, D. Sheptyakov, B. Batlogg and H. Ott, Phys. Rev. Lett., 2013, **110**, 266401.

[20] Z. Lu and J. Dahn, J. Electrochem. Soc., 2001, **148**, A1225.

[21] N. Yabuuchi, K. Kubota, M. Dahbi and S. Komaba, Chem. Rev., 2014, **114**, 11636-11682.

[22] L. Wang, Y. G. Sun, L. L. Hu, J. Y. Piao, J. Guo, A. Manthiram, J. Ma and A. M. Cao, J. Mater. Chem. A, 2017, **5**, 8752-8761.

[23] C. Wang, L. Liu, S. Zhao, Y. Liu, Y. Yang, H. Yu, S. Lee, G. H. Lee, Y. M. Kang and R. Liu, Nat. Commun., 2021, **12**, 1-9.

[24] T. Jin, P. F. Wang, Q. C. Wang, K. Zhu, T. Deng, J. Zhang, W. Zhang, X. Q. Yang, L. Jiao and C. Wang, Angew. Chem., 2020, **132**, 14619-14624.

[25] B. Peng, Y. Chen, F. Wang, Z. Sun, L. Zhao, X. Zhang, W. Wang and G. Zhang, Adv. Mater., 2021, **34**, 2103210.

[26] X. Li, D. Wu, Y. N. Zhou, L. Liu, X. Q. Yang and G. Ceder, Electrochem commun., 2014, **49**, 51-54.

[27] A. Sarkar, L. Velasco, D. Wang, Q. Wang, G. Talasila, L. de Biasi, C. Kübel, T. Brezesinski, S. S. Bhattacharya and H. Hahn, Nat. Commun., 2018, **9**, 1-9.

[28] J. Gild, M. Samiee, J. L. Braun, T. Harrington, H. Vega, P. E. Hopkins, K. Vecchio and J. Luo, J. Eur. Ceram. Soc., 2018, **38**, 3578-3584.

[29] C. M. Rost, E. Sachet, T. Borman, A. Moballegh, E. C. Dickey, D. Hou, J. L. Jones, S. Curtarolo and J. P. Maria, Nat. Commun., 2015, **6**, 1-8.

[30] S. Jiang, T. Hu, J. Gild, N. Zhou, J. Nie, M. Qin, T. Harrington, K. Vecchio and J. Luo, Scr. Mater., 2018, **142**, 116-120.

[31] D. Wang, S. Jiang, C. Duan, J. Mao, Y. Dong, K. Dong, Z. Wang, S. Luo, Y. Liu and X. Qi, J. Alloys Compd., 2020, **844**, 156158.

[32] D. Bérardan, S. Franger, A. Meena and N. Dragoe, J. Mater. Chem. A, 2016, **4**, 9536-9541.

[33] K. H. Tian, C. Q. Duan, Q. Ma, X. L. Li, Z. Y. Wang, H. Y. Sun, S. H. Luo, D. Wang and Y. G. Liu, Rare Metals, 2021, **41**, 1265-1275.

[34] Q. Wang, A. Sarkar, D. Wang, L. Velasco, R. Azmi, S. S. Bhattacharya, T. Bergfeldt, A. Düvel, P. Heitjans and T. Brezesinski, Energy Environ. Sci., 2019, **12**, 2433-2442.

[35] C. Zhao, F. Ding, Y. Lu, L. Chen and Y. Hu, Angew. Chem. Int. Ed., 2020, **59**, 264-269.

[36] Q. C. Wang, J. K. Meng, X. Y. Yue, Q. Q. Qiu, Y. Song, X. J. Wu, Z. W. Fu, Y. Y. Xia, Z. Shadike and J. Wu, J. Am. Chem. Soc., 2018, **141**, 840-848.

[37] P. F. Wang, Y. Xiao, N. Piao, Q. C. Wang, X. Ji, T. Jin, Y. J. Guo, S. Liu, T. Deng and C. Cui, Nano Energy, 2020, **69**, 104474.

[38] Q. C. Wang, E. Hu, Y. Pan, N. Xiao, F. Hong, Z. W. Fu, X. J. Wu, S. M. Bak, X. Q. Yang and Y. N. Zhou, Adv. Sci., 2017, **4**, 1700219.

[39] Y. N. Zhou, J. Ma, E. Hu, X. Yu, L. Gu, K. W. Nam, L. Chen, Z. Wang and X. Q. Yang, Nat. Commun., 2014, **5**, 1-8.

[40] Q. C. Wang, Z. Shadike, X. L. Li, J. Bao, Q. Q. Qiu, E. Hu, S. M. Bak, X. Xiao, L. Ma and X. J. Wu, Adv. Energy Mater., 2021, **11**, 2003455.

[41] X. L. Li, J. Bao, Y. F. Li, D. Chen, C. Ma, Q. Q. Qiu, X. Y. Yue, Q. C. Wang and Y. N. Zhou, Adv. Sci., 2021, **8**, 2004448.

[42] D. A. Anang, J. H. Park, D. S. Bhange, M. K. Cho, W. Y. Yoon, K. Y. Chung and K. W. Nam, Ceram. Int., 2019, **45**, 23164-23171.

[43] J. L. Yue, Y. N. Zhou, X. Yu, S. M. Bak, X. Q. Yang and Z. W. Fu, J. Mater. Chem. A, 2015, **3**, 23261-23267.

[44] P. Zhang, M. Chen, X. Shen, Q. Wu, X. Zhang, L. Huan and G. Diao, Electrochim. Acta, 2016, **204**, 92-99.

[45] N. T. Suen, S. P. Guo, J. Hoos and S. Bobev, Inorg. Chem., 57 (2018) 5632-5641.

[46] Y. Xie, H. Wang, G. Xu, J. Wang, H. Sheng, Z. Chen, Y. Ren, C. J. Sun, J. Wen and J. Wang, Adv. Energy Mater., 2016, **6**, 1601306.

[47] S. Zheng, G. Zhong, M. J. McDonald, Z. Gong, R. Liu, W. Wen, C. Yang and Y. Yang, J. Mater. Chem. A, 2016, **4**, 9054-9062.

[48] S. Komaba, N. Yabuuchi, T. Nakayama, A. Ogata, T. Ishikawa and I. Nakai, Inorg. Chem., 2012, **65**, 1211-6220.

[49] Y. Chen, C. Qian, P. Zhang, R. Zhao, J. Lu and M. Chen, J. Electroanal. Chem., 2018, **815**, 123-129.

[50] M. H. Wang, Z. Ma, H. G. Xue and S. P. Guo, Inorg. Chem. Front., 2018, **5**, 2306-2313.